Optical phonons in a periodically inverted polar superlattice

Jing Chen and Jacob B. Khurgin
Department of Electrical & Computer Engineering, Johns Hopkins University, Baltimore, Maryland 21218, USA
(Received 13 June 2003; revised manuscript received 25 March 2004; published 31 August 2004)

Optical lattice vibrations in a zinc-blende superlattice consisting of periodically inverted polar domains are theoretically investigated and phonon dispersion curves are obtained. The salient features of the phonon dispersion are the mixing of longitudinal and transverse optical phonons and zone folding at twice the superlattice wave vector. The patterns of sublattice displacement and electric field are obtained and analyzed. The most interesting feature is the change in symmetry between the displacement and the electrical field, leading to different selection rules for various photon-phonon and carrier-phonon interactions.

DOI: 10.1103/PhysRevB.70.085319 PACS number(s): 68.65.Cd, 63.22.+m, 63.20.Dj

I. INTRODUCTION

Rapid progress of nanoscale growth and fabrication techniques over the past 20 years[1] have brought us to the point where artificial materials with prescribed electrical and optical properties can be successfully engineered. Numerous successful optical and electronic devices based on unique properties of electrons in quantum wells and superlattices have been developed.[2] Just as the electrons, the lattice vibrations also exhibit different characteristics when confined in one or more directions. However these changes have not yet found application in devices. Among the different modes of lattice vibrations, long wavelength optical phonons are probably the most important when it comes to electronic devices which are based on III-V semiconductors. The reason for this is that longitudinal optical phonon (LO) scattering is the dominant mechanism restricting the hot carrier's mobility, and hence any substantial modification of optical phonon properties can lead to a significant improvement in their performance.[3]

There has been considerable work performed on the properties of confined optical phonons in various structures.[4–6] Among the different developed models the phenomenological continuum model[4,6] has been most successful in explaining the properties of optical phonons in various heterostructures where different layers have different phonon frequencies, such as GaAs/AlAs. In such structures one can safely assume that the vibrational modes are confined to one layer and that the only connection between adjacent modes is the electrostatic potential so that the dispersion curves of the phonons in the plane of growth are modified. Unfortunately this is not of practical interest since in realistic electronic and optical devices it is desirable to remove the optical phonons as fast as possible towards the heat sink, i.e., in the direction normal to the plane of growth. It is, therefore, interesting to explore heterostructures in which the phonons can move in three dimensions with modified dispersion. In order to have phonons travel freely throughout the heterostructure, it is necessary that the elastic properties and polarizabilities of alternating layers be the same. This means that in terms of the magnitudes of all the relevant material parameters, the alternating layers must be identical. This leaves us with the freedom of changing the sign of the parameters and brings forward the idea of using a periodically inverted polar domain structure (PIPDS)—a concept well known in the field of nonlinear optics, where it is called a "quasi-phase-matched (QPM) structure."[7]

The QPM concept is based on the fact that if a crystal lacks a center of inversion symmetry, inversion will lead to a sign reversal of odd-order tensor elements, including, for example, the second-order optical susceptibility $\chi^{(2)}$. The QPM structure is a superlattice of alternating inverted layers. Hence when light of frequency ω and wave vector $\boldsymbol{k}(\omega)$ propagates in this structure, the nonlinear polarization at the second-harmonic frequency 2ω can be represented as a superposition of waves with wave vectors $2\boldsymbol{k}(\omega)+n\boldsymbol{q}_0$, where n is an integer, $\boldsymbol{q}_0=2\pi/\Lambda\hat{z}$ is the superlattice wave vector, Λ is the period of the QPM structure, and $\hat{z}$ is the unit vector in the direction of growth. If one of the wave vectors matches that of the second-harmonic electromagnetic wave $\boldsymbol{k}(2\omega)$ (preferably the lowest order), an efficient transfer of energy into the second harmonic will ensue. The QPM structure thus provides significant modification of the nonlinear optical properties of the material while leaving the linear optical properties intact. If, as often is the case, the QPM structure is made of ferroelectric materials such as $LiNbO_3$, domain reversal can be achieved using electrical field poling from an already grown crystal. For zinc-blende semiconductors such as GaAs and ZnSe, which are not ferroelectric, one must resort to more challenging crystal growth methods such as stacking of plates approach, wafer bonding, and all-epitaxy fabrication.[8]

It is of fundamental interest to look at the optical phonons in the zinc-blende semiconductor PIPDS. While no third-order tensors are directly involved in the interaction of the phonon with light and electrons, the dynamic effective ionic charge $\boldsymbol{e}^*$ (Ref. 9) does reverse its sign upon crossing a domain boundary. As a result, momentum conservation rules for such processes as infrared absorption and the Fröhlich interaction change drastically, and large wave-vector optical phonons, which are difficult to produce in bulk crystals, can be easily generated in PIPDS, as will be shown in the present paper. While conceptually similar to a typical QPM structure, phonon PIPDS is distinguished by its finer scale. The domains are reversed every few lattice constants, i.e., on a nanometer scale.

We start by describing the microscopic structure of PIPDS as shown in Fig. 1. Since the bulk zinc-blende crystal struc-

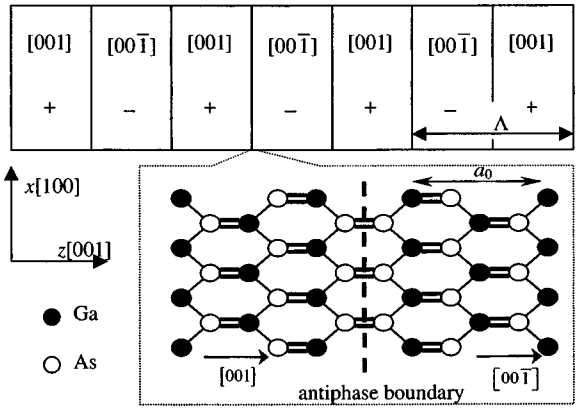

FIG. 1. Schematic diagram of an antiphase boundary for III–V semiconductors PIPDS among [001].

ture can be viewed as two perfect face-centered-cubic (fcc) sublattices A and B, domain inversion simply means that the cation and anion exchange the sublattices they occupy. This inversion is known to occur spontaneously in "rotational twins"[10] and "antiphase boundaries"[11] in some zinc-blende compounds. Such artificial domains have been successfully operated in "orientation-patterned structures."[8] While the domain reversal in III-V semiconductors more often occurs along the [011] directions,[8,11] nothing in principle prevents it from taking place along one of the [001] directions. In this work we will consider an III-V semiconductor PIPDS oriented along [001] axis as shown in Fig. 1. If we define a phonon as a vibrational mode of relative displacement between sublattices A and B, the ionic polarization $\boldsymbol{P}$ will have identical amplitudes but opposite signs at two adjacent domains. If the optical phonon mode can be represented by amplitude $\boldsymbol{u}_0(\boldsymbol{q})$ with wave vector $\boldsymbol{q}$, the polarization wave $\boldsymbol{P}$ associated with this phonon mode will contain components with wave vectors $\boldsymbol{q}'=\boldsymbol{q}+n\boldsymbol{q}_0$, where n is an integer. The electric field excited by this polarization $\boldsymbol{P}$ will, in turn, be able to apply force to the other phonon modes with wave vectors $\boldsymbol{q}''=\boldsymbol{q}'+m\boldsymbol{q}_0=\boldsymbol{q}+(m+n)\boldsymbol{q}_0$ (the PIPDS Bragg condition). Such a coupling mechanism will lead to the modification of the optical phonon dispersion curves in PIPDS while leaving the elastic properties almost intact. This is precisely the goal that we are trying to achieve, that is to have optical phonons propagating freely in all directions with modified dispersion curves.

To obtain insight into the optical phonon properties in III-V semiconductor PIPDS we have developed a simplified theoretical description using a "nearly free phonon" formalism in Sec. II. In Sec. III we obtain analytical results for special cases such as the zero dispersion and long wave limits, while in Sec. IV dispersion results for phonons with arbitrary wave vectors are generated numerically and analyzed. The issue of interactions between optical phonons and photons and/or electrons in PIPDS are addressed in Sec. V. Conclusions are presented in Sec. VI.

II. THEORETICAL MODEL OF PHONONS IN PIPDS

The so-called "continuum" model of a III-V semiconductor PIPDS is shown in Fig. 1. The domains are inverted with period $\Lambda=Ma_0$, where a_0 is the fcc lattice constant, which is twice the value for a primitive cell, and M is an integer. Thus, in theory the Brillouin zone (BZ) of the bulk material $(-2\pi/a_0, 2\pi/a_0)$ is split into exactly $2M$ folded zones of the superstructure $(-\pi/Ma_0, \pi/Ma_0)$. As will become clear below, it is reasonable to use the modified BZ $(-2\pi/Ma_0, 2\pi/Ma_0)$.

Due to the periodic inversion, the relation between relative sublattice displacement and polarization in this structure are modulated by a periodical square wave function f

$$f(z)=\begin{cases}+1; & n\Lambda<z<(n+0.5)\Lambda\\ -1; & (n-0.5)\Lambda<z<n\Lambda,\end{cases} \tag{1a}$$

where n is an integer. One can also say that Eq. (1a) describes the modulation of the dynamic effective ionic charges $\boldsymbol{e}^*$ (Ref. 9). This envelope function f can be expanded into a Fourier series as

$$f(z)=\sum_{n=-\infty}^{\infty} g_n \exp(inq_0 z)=\sum_{n\pm1,\pm3\ldots}\left(-i\frac{2}{\pi n}\right)\exp(in\boldsymbol{q}_0\cdot\boldsymbol{r}), \tag{1b}$$

where $\boldsymbol{q}_0=2\pi/\Lambda\hat{z}$ is the superlattice wave vector. It should be mentioned that we shall only consider structures with identical widths of "positive" and "negative" domains, i.e., having a definite symmetry. Then the envelope function f has only odd Fourier components. Hence, calculation of the dispersion curves (Secs. III and IV) and the discussion of the selection rules for the photon-phonon and electron-phonon interactions (Sec. V) can be substantially simplified.

Further simplifications have been made in developing our model. First, the mechanical properties of the material are assumed not to be influenced by the existence of the domain boundary. This is indeed a major simplification since the cation and anion have different masses. However, if their masses are close to each other, this discrepancy (7% for GaAs) can be handled later as a small perturbation. Furthermore, nonpolar Ga-Ga and As-As bonds that exist at the antiphase boundary have different elastic properties than in heteropolar Ga-As bonds. With the ionicity of the Ga-As bond[12] being only about 20% one can still treat the deviation in bond character as a perturbation, whose main impact is the opening of small gaps at the edge of the folded BZ. Of course, interface phonon modes associated with the Ga-Ga and As-As bonds can also exist, but since the bands are nonpolar they will not make a large impact on the infrared and electron scattering properties that are of interest here. Finally, in this work we will consider rather small domains, only a few primitive cells thick. Therefore, using a macroscopic description for the polarization is definitely an approximation and all the results obtained in this paper are just estimates. However, using this macroscopic approximation allows us to develop a rather clear qualitative picture of the physical processes in PIPDS and to obtain solutions that do not require

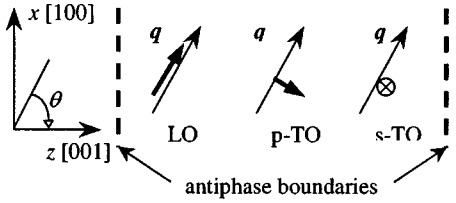

FIG. 2. Basis of phonon modes in PIPDS.

extensive numerical computations and which can be easily interpreted for the high symmetry directions.

Having established the limitations of our approach, we now commence our study with the use of the macroscopic Huang-Born equations[6,13]

$$\ddot{\boldsymbol{u}} = -\omega_T^2 \boldsymbol{u} + b_{12} f \boldsymbol{E} - \beta_L^2 \nabla\nabla\cdot\boldsymbol{u} + \beta_T^2 \nabla\times\nabla\times\boldsymbol{u}, \quad (2a)$$

$$\nabla\cdot\boldsymbol{D} = \nabla\cdot(b_{21} f \boldsymbol{u} + \varepsilon_0\varepsilon_\infty \boldsymbol{E}) = 0, \quad (2b)$$

where $\boldsymbol{u} = \sqrt{M_r/\Omega}\boldsymbol{u}_0$ is the modified relative sublattice displacement, M_r is the reduced mass of the anion-cation pair, Ω is the unit-cell volume, $\boldsymbol{E}$ is the macroscopic electrical field, $b_{21} = b_{21} = \sqrt{\varepsilon_0\varepsilon_\infty(\omega_L^2 - \omega_T^2)}$, $\omega_{L/T}$ is the BZ center angular frequency of the bulk longitudinal/transverse optical (LO/TO) phonon, ε_∞ is the optical frequency dielectric constant, ε_0 is the vacuum permittivity, and $\beta_{L/T}$ is a phenomenological parameter describing the curvature of the LO/TO phonon dispersion.

Equation (2) can be simplified by considering three orthogonal sublattice vibration modes as shown in Fig. 2.[4] Here the bold arrow labels the direction of relative sublattice displacement. The mode polarized among wave vector $\boldsymbol{q}$ is referred to as the LO mode, the mode whose polarization lies in the plane formed by z and $\boldsymbol{q}$ [plane (010) here] is called the p-TO mode and the last one, polarized along the y [010] direction is called the shear horizontal (s-TO mode). Since the domain inversion does not change the mechanical properties of the bulk material, clearly the s-TO mode will remain essentially a bulk TO mode. Another way to understand this is to invoke the tangential electric field (E_x, E_y) and normal electric displacement D_z, all of which are zero for the bulk s-TO mode. On the other hand, the LO and p-TO modes both produce a discontinuous polarization $\boldsymbol{P}$ at the antiphase boundaries. Thus, in PIPDS the LO($\boldsymbol{q}$) and p-TO($\boldsymbol{q}$) modes will couple together as well as to other LO PIPDS Bragg condition. Thus, we shall focus our attention only on these coupled LO-p-TO modes in the (010) plane.

To determine the dispersion of the mixed LO-p-TO modes, we shall expand the modified relative sublattice displacement $\boldsymbol{u}$ using basis as the bulk LO and p-TO modes, i.e.,

$$\boldsymbol{u} = \sum_{\boldsymbol{q}} (C_{\boldsymbol{q}}^L \boldsymbol{a}_{\boldsymbol{q}}^L + C_{\boldsymbol{q}}^T \boldsymbol{a}_{\boldsymbol{q}}^T)\exp(i\mathbf{q}\cdot\mathbf{r} - i\omega t), \quad (3)$$

where $\boldsymbol{a}_{\boldsymbol{q}}^{L/T}$ is the unit polarization vector of the LO (p-TO) mode.

Next, we introduce the "charge displacement" as $\boldsymbol{w} = f\boldsymbol{u}$, which in fact is the "true" modified relative displacement between cations and anions. Using Eq. (1b) and Eq. (3) we can expand the charge displacement $\boldsymbol{w}$ in the same basis as for the modified relative sublattice displacement $\boldsymbol{u}$

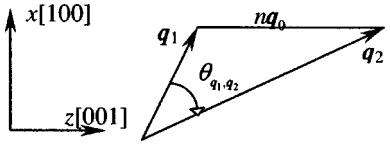

FIG. 3. Illustration of rotation.

$$\begin{aligned}\boldsymbol{w} &= \sum_{n=\pm1,\pm3\ldots}\sum_{\boldsymbol{q}} g_n(C_{\boldsymbol{q}}^L \boldsymbol{a}_{\boldsymbol{q}}^L + C_{\boldsymbol{q}}^T \boldsymbol{a}_{\boldsymbol{q}}^T) e^{i\mathbf{q}\cdot\mathbf{r} - i\omega t + in\mathbf{q}_0\cdot\mathbf{r}} \\ &= \sum_{\boldsymbol{q}_1}\sum_{n=\pm1,\pm3\ldots} g_n(C_{\boldsymbol{q}_1 - n\boldsymbol{q}_0}^L \boldsymbol{a}_{\boldsymbol{q}_1 - n\boldsymbol{q}_0}^L + C_{\boldsymbol{q}_1 - n\boldsymbol{q}_0}^T \boldsymbol{a}_{\boldsymbol{q}_1 - n\boldsymbol{q}_0}^T) e^{i\boldsymbol{q}_1\cdot\mathbf{r} - i\omega t} \\ &= \sum_{\boldsymbol{q}_1} (D_{\boldsymbol{q}_1}^L \boldsymbol{a}_{\boldsymbol{q}_1}^L + D_{\boldsymbol{q}_1}^T \boldsymbol{a}_{\boldsymbol{q}_1}^T) e^{i\boldsymbol{q}_1\cdot\mathbf{r} - i\omega t}, \end{aligned} \quad (4a)$$

where we have introduced $\boldsymbol{q}_1 = \boldsymbol{q} + n\boldsymbol{q}_0$, n being an odd integer. Here

$$\begin{aligned} D_{q_1}^L = \sum_{n=\pm1,\pm3\ldots} g_n(&C_{\boldsymbol{q}_1 - n\boldsymbol{q}_0}^L \cos\theta_{\boldsymbol{q}_1 - n\boldsymbol{q}_0, \boldsymbol{q}_1} \\ &+ C_{\boldsymbol{q}_1 - n\boldsymbol{q}_0}^T \sin\theta_{\boldsymbol{q}_1 - n\boldsymbol{q}_0, \boldsymbol{q}_1}), \end{aligned} \quad (4b)$$

$$\begin{aligned} D_{\boldsymbol{q}_1}^T = \sum_{n=\pm1,\pm3\ldots} g_n(&- C_{\boldsymbol{q}_1 - n\boldsymbol{q}_0}^L \sin\theta_{\boldsymbol{q}_1 - n\boldsymbol{q}_0, \boldsymbol{q}_1} \\ &+ C_{\boldsymbol{q}_1 - n\boldsymbol{q}_0}^T \cos\theta_{\boldsymbol{q}_1 - n\boldsymbol{q}_0, \boldsymbol{q}_1}), \end{aligned} \quad (4c)$$

where $\theta_{\boldsymbol{q}_1,\boldsymbol{q}_2}$ is the rotation angle from $\boldsymbol{q}_1$ to $\boldsymbol{q}_2$, as shown in Fig. 3 and the positive direction is set to be clockwise.

Now we can rewrite the Eq. (2b) as $\nabla\cdot(b_{12}\boldsymbol{w} + \varepsilon_0\varepsilon_\infty\boldsymbol{E}) = 0$. According to Eq. (4a) the charge displacement $\boldsymbol{w}$ is a superposition of independent longitudinal and transverse plane waves. The longitudinal waves carry an electric field while the transverse modes do not.[13] The total electric field $\boldsymbol{E}$ is then

$$\begin{aligned} \boldsymbol{E} &= -\frac{b_{12}}{\varepsilon_0\varepsilon_\infty}\sum_{\boldsymbol{q}_1} D_{\boldsymbol{q}_1}^L \boldsymbol{a}_{\boldsymbol{q}_1}^L e^{i\boldsymbol{q}_1\cdot\mathbf{r} - i\omega t} \\ &= -\frac{b_{12}}{\varepsilon_0\varepsilon_\infty}\sum_{n=\pm1,\pm3\ldots}\sum_{\boldsymbol{q}} g_n(C_{\boldsymbol{q}}^L \cos\theta_{\boldsymbol{q},\boldsymbol{q}+n\boldsymbol{q}_0} \\ &\quad + C_{\boldsymbol{q}}^T \sin\theta_{\boldsymbol{q},\boldsymbol{q}+n\boldsymbol{q}_0}) \boldsymbol{a}_{\boldsymbol{q}+n\boldsymbol{q}_0}^L e^{i\boldsymbol{q}\cdot\mathbf{r} + in\mathbf{q}_0\cdot\mathbf{r} - i\omega t}. \end{aligned} \quad (5)$$

Next we substitute Eq. (5) and Eq. (3) into Eq. (2a), multiply both sides by $\exp(-i\boldsymbol{q}_1\cdot\boldsymbol{r})$, integrate over the volume, and finally evaluate scalar products with $\boldsymbol{a}_{\boldsymbol{q}_1}^{L/T}$ to obtain

$$(\omega^2-\omega_T^2+\beta_L^2\boldsymbol{q}_1^2)C^L_{\boldsymbol{q}_1}=(\omega_L^2-\omega_T^2)\sum_{m=0,\pm2\ldots}\sum_{n=\pm1,\pm3\ldots}g_{m-n}g_n\cos\theta_{\boldsymbol{q}_1,\boldsymbol{q}_1-n\boldsymbol{q}_0}\times(C^L_{\boldsymbol{q}_1-m\boldsymbol{q}_0}\cos\theta_{\boldsymbol{q}_1-m\boldsymbol{q}_0,\boldsymbol{q}_1-n\boldsymbol{q}_0}+C^T_{\boldsymbol{q}_1-m\boldsymbol{q}_0}\sin\theta_{\boldsymbol{q}_1-m\boldsymbol{q}_0,\boldsymbol{q}_1-n\boldsymbol{q}_0}),\tag{6a}$$

$$(\omega^2-\omega_T^2+\beta_T^2\boldsymbol{q}_1^2)C^T_{\boldsymbol{q}_1}=(\omega_L^2-\omega_T^2)\sum_{m=0,\pm2\ldots}\sum_{n=\pm1,\pm3\ldots}g_{m-n}g_n\sin\theta_{\boldsymbol{q}_1,\boldsymbol{q}_1-n\boldsymbol{q}_0}\times(C^L_{\boldsymbol{q}_1-m\boldsymbol{q}_0}\cos\theta_{\boldsymbol{q}_1-m\boldsymbol{q}_0,\boldsymbol{q}_1-n\boldsymbol{q}_0}+C^T_{\boldsymbol{q}_1-m\boldsymbol{q}_0}\sin\theta_{\boldsymbol{q}_1-m\boldsymbol{q}_0,\boldsymbol{q}_1-n\boldsymbol{q}_0}).\tag{6b}$$

Now we can move the diagonal terms with $m=0$ from the right-hand side (rhs) of Eq. (6) to the left-hand side (lhs), while dropping the subscript "1" in the wave vector and defining the new parameters as

$$\eta_q=\sum_{n=\pm1,\pm3\ldots}g_ng_{-n}\cos^2\theta_{\boldsymbol{q},\boldsymbol{q}-n\boldsymbol{q}_0},\tag{7a}$$

$$\chi_q=\sum_{n=\pm1,\pm3\ldots}g_ng_{-n}\sin\theta_{\boldsymbol{q},\boldsymbol{q}-nq_0}\cos\theta_{\boldsymbol{q},\boldsymbol{q}-n\boldsymbol{q}_0},\tag{7b}$$

$$\alpha^{LL}_{\boldsymbol{q},m}=\sum_{n=\pm1,\pm3\ldots}g_{m-n}g_n\cos\theta_{\boldsymbol{q}-m\boldsymbol{q}_0,q-n\boldsymbol{q}_0}\cos\theta_{\boldsymbol{q}-n\boldsymbol{q}_0,q},\tag{7c}$$

$$\alpha^{LT}_{\boldsymbol{q},m}=\sum_{n=\pm1,\pm3\ldots}g_{m-n}g_n\cos\theta_{\boldsymbol{q}-m\boldsymbol{q}_0,\boldsymbol{q}-n\boldsymbol{q}_0}\sin\theta_{\boldsymbol{q}-n\boldsymbol{q}_0,\boldsymbol{q}},\tag{7d}$$

$$\alpha^{TL}_{\boldsymbol{q},m}=\sum_{n=\pm1,\pm3\ldots}g_{m-n}g_n\sin\theta_{\boldsymbol{q}-m\boldsymbol{q}_0,\boldsymbol{q}-n\boldsymbol{q}_0}\cos\theta_{\boldsymbol{q}-n\boldsymbol{q}_0,q},\tag{7e}$$

$$\alpha^{TT}_{\boldsymbol{q},m}=\sum_{n=\pm1,\pm3\ldots}g_{m-n}g_n\sin\theta_{\boldsymbol{q}-m\boldsymbol{q}_0,\boldsymbol{q}-n\boldsymbol{q}_0}\sin\theta_{\boldsymbol{q}-n\boldsymbol{q}_0,\boldsymbol{q}},\tag{7f}$$

where m should be even integers. We finally have the characteristic equations for the phonon dispersion in PIPDS

$$[\omega^2+\beta_L^2q^2-\eta_{\boldsymbol{q}}\omega_L^2-(1-\eta_{\boldsymbol{q}})\omega_T^2]C^L_{\boldsymbol{q}}-(\omega_L^2-\omega_T^2)\chi_{\boldsymbol{q}}C^T_{\boldsymbol{q}}=(\omega_L^2-\omega_T^2)\sum_{m=\pm2,\pm4\ldots}(\alpha^{LL}_{\boldsymbol{q},m}C^L_{\boldsymbol{q}-m\boldsymbol{q}_0}+\alpha^{LT}_{\boldsymbol{q},m}C^T_{\boldsymbol{q}-m\boldsymbol{q}_0}),\tag{8a}$$

$$[\omega^2+\beta_T^2q^2-\eta_{\boldsymbol{q}}\omega_T^2-(1-\eta_{\boldsymbol{q}})\omega_L^2]C^T_{\boldsymbol{q}}-(\omega_L^2-\omega_T^2)\chi_{\boldsymbol{q}}C^L_{\boldsymbol{q}}=(\omega_L^2-\omega_T^2)\sum_{m=\pm2,\pm4\ldots}(\alpha^{TL}_{\boldsymbol{q},m}C^L_{\boldsymbol{q}-m\boldsymbol{q}_0}+\alpha^{TT}_{\boldsymbol{q},m}C^T_{\boldsymbol{q}-m\boldsymbol{q}_0}),\tag{8b}$$

where we have used the fact that $\Sigma_{n=-\infty}^{\infty}g_ng_{-n}=1$.

As one can see, only the vibrations whose wave vectors differ by an even number of superlattice wave vectors $\boldsymbol{q}_0$, i.e., $4\pi/\Lambda$, are coupled together. Therefore, we can indeed use the modified BZ $(-2\pi/Ma_0, 2\pi/Ma_0)$. This modified Bragg condition is quite different from the Bragg condition in ordinary periodic structure, which can be easily understood from the original Eq. (2). Excluding the electric field from them immediately shows that the solution should have periodicity of the function $f^2(z)$, i.e., $\Lambda/2$, which is M primitive cell constants. Therefore, to determine the coupled LO-p-TO optical phonon dispersion one needs to diagonalize a $2M\times2M$ matrix, which, generally speaking, can only be done numerically. However, before proceeding with the numerical calculations, in the next section we will consider some special cases which will allow us to gain some physical insight into PIPDS phonon properties.

III. SPECIAL CASES

A. Zero dispersion $\beta_L=\beta_T=0$

Neglecting optical phonon dispersion implies that each anion-cation pair acts as an independent oscillator. Then the oscillation phases of two bonds at two sides of the antiphase boundary can simply be reversed to satisfy the electrostatic boundary conditions. Equation (2) can be rewritten in terms of the charge displacement $\boldsymbol{w}$ as

$$\ddot{\boldsymbol{w}}=-\omega_T^2\boldsymbol{w}+b_{12}\boldsymbol{E},\tag{9a}$$

$$\nabla\cdot\boldsymbol{D}=\nabla\cdot(b_{21}\boldsymbol{w}+\varepsilon_0\varepsilon_\infty\boldsymbol{E})=0.\tag{9b}$$

These expressions are identical to the Huang-Born equations in bulk dispersionless materials.[13] Therefore, if one redefines the PIPDS optical phonon in terms of charge displacement $\boldsymbol{w}$ rather than the relative sublattices displacement $\boldsymbol{u}_0$, the optical phonon properties in PIPDS would be indistinguishable from the bulk optical phonon properties.

B. On-axis propagation $q_x=0$

In this case all the wave vectors $\boldsymbol{q}-m\boldsymbol{q}_0$ are collinear, hence $\sin\theta_{\boldsymbol{q},\boldsymbol{q}-m\boldsymbol{q}_0}=0$, so that $\chi_{\boldsymbol{q}}=\alpha^{\mathrm{LT}}_{\boldsymbol{q},m}=\alpha^{\mathrm{TL}}_{\boldsymbol{q},m}=\alpha^{\mathrm{TT}}_{\boldsymbol{q},m}=0$. Furthermore, since $\Sigma_ng_{n-m}g_n=-\delta_{m,0}$, the remaining off-diagonal components $\alpha^{LL}_{\boldsymbol{q},m}$ are also equal to zero, while all the $\eta_{\boldsymbol{q}}=1$ and we are left only with a diagonal matrix whose eigenvalues are

$$\omega^2=\omega_L^2-\beta_L^2q^2\quad(\text{LO mode}),\tag{10a}$$

$$\omega^2=\omega_T^2-\beta_T^2q^2\quad(\text{p-TO mode}).\tag{10b}$$

We see that in this case the LO mode and p-TO mode are decoupled from each other and exhibit the same dispersion properties as in bulk materials, with no gaps at the edge of the modified BZ. This is an expected result, since the LO and p-TO modes propagating along z do not carry an electric field $\boldsymbol{E}_\parallel$ parallel to the boundary nor an electric displacement $\boldsymbol{D}_z$ normal to the boundary. Furthermore, the p-TO and s-TO modes are degenerate for the on-axis propagation case. Note that this result is only an approximation since small mass difference between the anion and cation will open narrow gaps at the BZ edge and center, but as mentioned before, we disregard this effect here.

C. Long wave limit $q\to0$

For $\boldsymbol{q}\ll\boldsymbol{q}_0$ it is rather easy to see that the wave vectors $\boldsymbol{q}-m\boldsymbol{q}_0$ are also all nearly collinear. Then we can obtain

$$\sin\theta_{\mathbf{q}-m\mathbf{q}_0,\mathbf{q}-n\mathbf{q}_0}=0,\quad m,n\neq 0,$$

$$\cos\theta_{\mathbf{q}-m\mathbf{q}_0,\mathbf{q}-n\mathbf{q}_0}=\mathrm{sign}(m)\mathrm{sign}(n),\quad m,n\neq 0,$$

$$\sin\theta_{\mathbf{q},\mathbf{q}-n\mathbf{q}_0}=-\mathrm{sign}(n)\sin\theta,$$

$$\cos\theta_{\mathbf{q},\mathbf{q}-n\mathbf{q}_0}=-\mathrm{sign}(n)\cos\theta, \tag{11a}$$

where θ is the rotation angle from $\boldsymbol{q}$ to $\boldsymbol{z}$, and sign(n) is +1 if $n>0$ and −1 for $n<0$. Hence,

$$\alpha^{LL}_{\mathbf{q},m}=\alpha^{LT}_{\mathbf{q},m}=\alpha^{TL}_{\mathbf{q},m}=\alpha^{TT}_{\mathbf{q},m}=0,$$

$$\chi_{\mathbf{q}}=\cos^2\theta,\quad \eta_{\mathbf{q}}=-\sin\theta\cos\theta. \tag{11b}$$

One then sees that the LO($\boldsymbol{q}$) and p-TO($\boldsymbol{q}$) modes are decoupled from the other modes and the secular equation between them simply becomes

$$\begin{vmatrix} \omega^2-\overline{\omega^2}-\dfrac{\omega_L^2-\omega_T^2}{2}\cos 2\theta & \dfrac{\omega_L^2-\omega_T^2}{2}\sin 2\theta \\ \dfrac{\omega_L^2-\omega_T^2}{2}\sin 2\theta & \omega^2-\overline{\omega^2}+\dfrac{\omega_L^2-\omega_T^2}{2}\cos 2\theta \end{vmatrix} = 0, \tag{12}$$

where $\overline{\omega^2}=(\omega_L^2+\omega_T^2)/2$.

It is easy to verify that Eq. (12) always gives the same eigenvalues but that the eigenvectors do change for different θ, as

$$\omega_+=\omega_L\Rightarrow \boldsymbol{u}_{\mathbf{q}}=\cos\theta\boldsymbol{a}^L_{\mathbf{q}}+\sin\theta\boldsymbol{a}^T_{\mathbf{q}}=\hat{z}, \tag{13a}$$

$$\omega_-=\omega_T\Rightarrow \boldsymbol{u}_{\mathbf{q}}=\sin\boldsymbol{a}^L_{\mathbf{q}}-\cos\theta\boldsymbol{a}^T_{\mathbf{q}}=\hat{\boldsymbol{x}}. \tag{13b}$$

Once again the result is expected. For small wave vectors the electrostatic potential and electric field are determined by modulation of the charge displacement $\boldsymbol{w}$ imposed by domain reversal. Therefore, it is relative to the z direction that phonons will split into transverse and longitudinal branches.

Equation (13) indicates a very interesting fact for the two extreme situations, $\theta=0°$ and $\theta=90°$, for which the eigenmodes are indeed decoupled LO and p-TO modes and for which the higher frequency mode always has its sublattice displacement $\boldsymbol{u}$ along z direction. Thus for lateral propagation $\theta=90°$ it is the p-TO mode which possesses the higher frequency ω_L. This result will be confirmed by the numerical calculations in the following section.

TABLE I. Parameters for GaAs (Ref. 17).

ω_L (cm^{-1})	ω_T (cm^{-1})	a_0 (nm)	$\beta_L^2(10^{-12})$	$\beta_T^2(10^{-12})$
292	269	0.5653	2.91	3.12

IV. NUMERICAL RESULTS

Except for the special cases described in Sec. III, we have to resort to solving the full $2M\times 2M$ system of equations [Eq. (8)] to numerically generate dispersion curves for various directions, i.e., various angles θ between the phonon wave vector $\boldsymbol{q}$ and the growth direction z. We use GaAs as an example, with all the relevant material parameters for this material given in Table I. [Note that since $\omega_{L/T}$ are given in the same units (cm^{-1}) as q, the $\beta^2_{L/T}$ are dimensionless.] In performing the numerical calculations we set the following limitations on the wave vector $\boldsymbol{q}$, namely that q_z should be confined in the modified BZ $(-k_0/M,k_0/M)$, while the in-plane q_x belongs to the bulk BZ $(-k_0,k_0)$. Here $k_0=2\pi/a_0=1.11\times 10^8$ cm^{-1} for GaAs.

Numerically calculated dispersion curves for $M=5$ are shown in Fig. 4 for $\theta=90°$ and Fig. 5 for $\theta=45°$. Each figure consists of four plots: Plot (a) is the original spectrum of bulk GaAs phonons folded into the modified PIPDS BZ; plot

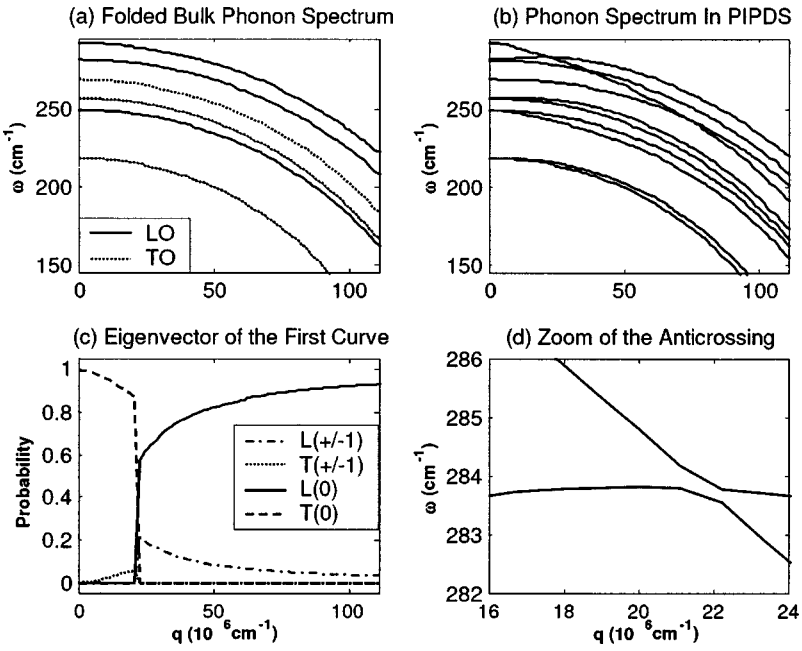

FIG. 4. Dispersion curves and eigenvectors in PIPDS for $M=5$ and $\theta=90°$.

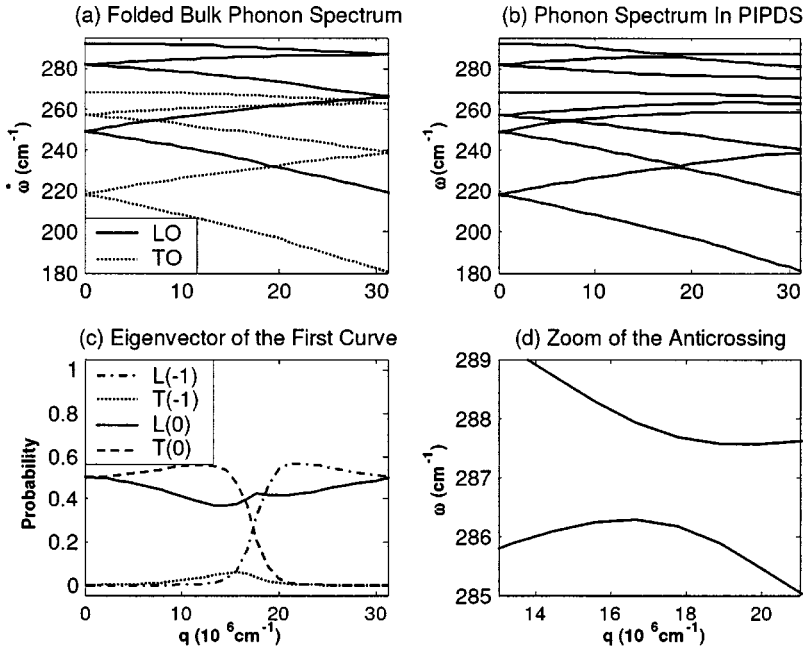

FIG. 5. Dispersion curves and eigenvectors in PIPDS for $M=5$ and $\theta=45°$.

(b) represents the numerically generated dispersion curves; plot (c) displays the composition (probabilities of constituent plane waves $|C^{L/T}_{q+mq_0}|^2$) of the highest frequency branch in plot (b) as a function of wave vector $\boldsymbol{q}$. Only the dominant-contributing modes are labeled in plot (c), with $L(m)$ corresponding to the LO($\boldsymbol{q}+2m\boldsymbol{q}_0$) mode and $T(m)$ corresponding to p-TO($\boldsymbol{q}+2m\boldsymbol{q}_0$) mode. Plot (d) displays a zoom in in the vicinity of the highest frequency anticrossing shown in plot (b).

Let us consider first the case in which the wave vector $\boldsymbol{q}$ is along the $\boldsymbol{x}$ [100] direction (lateral propagation), Fig. 4. In the long wave limit $q\rightarrow 0$, one can see from Fig. 4(c) that the highest frequency mode is essentially a bulk p-TO mode, just as expected according to the results of Sec. III, Eq. (13). This follows since the long wavelength longitudinal sublattices oscillations produce opposite polarizations $\boldsymbol{P}$ along the x direction in adjacent layers so that the fields generated by these polarizations will cancel each other out and contribute no additional restoring force to the sublattices. At the same time the p-TO oscillations produce polarization charges at the antiphase boundary. Thus, they experience an additional restoring force. Since it is this restoring force that causes the splitting of bulk LO and TO modes, one can understand why in this case the energies of long wave LO and p-TO phonons are reversed.

As the wave vector $\boldsymbol{q}$ increases, the contributions of the p-TO($\boldsymbol{q}\pm 2\boldsymbol{q}_0$) modes gradually arise, until following the anticrossing, the character of the mode changes abruptly to a combination of various LO modes. The anticrossing occurs in the vicinity of $q\sim 2.1\times 10^7$ cm$^{-1}\sim 0.95q_0$, which is to be expected since when $q\sim q_0$, the gradient of the charge displacement $\boldsymbol{w}$ and thus the electric field of both LO and p-TO vibrations is directed at roughly 45° to the axis z. This field exerts roughly equal electrostatic forces upon the oscillations of both LO and p-TO modes and thus mixes them. As the wave vector $\boldsymbol{q}$ increases past the anticrossing, the gradient of the charge displacement $\boldsymbol{w}$ approaches the direction of wave vector $\boldsymbol{q}$, and the lowest-order LO mode, LO($\boldsymbol{q}$), becomes dominant.

The dispersion curves for the cases when the wave vector $\boldsymbol{q}$ is not directed along $\boldsymbol{x}$ exhibit much stronger LO-p-TO phonon mixing, an example of which is shown in Fig. 5 for $\theta=45°$. When $\boldsymbol{q}$ is close to zero, the p-TO($\boldsymbol{q}$) and LO($\boldsymbol{q}$) modes dominate, and their probabilities are all 0.5 as follows from Eq. (13a). As the wave vector $\boldsymbol{q}$ increases, gradually the LO($\boldsymbol{q}-2\boldsymbol{q}_0$) mode starts contributing to the eigenvectors, while the p-TO($\boldsymbol{q}$) slowly vanishes. Eventually, when the wave vector $\boldsymbol{q}$ approaches the BZ edge, the highest energy state becomes a 50/50 combination of LO($\boldsymbol{q}$) and LO($\boldsymbol{q}-2\boldsymbol{q}_0$) modes with no contribution from other modes. Such a 50/50 combination can be easily explained by the Bragg reflection at the BZ boundary.

Having numerically calculated the eigenfrequencies and eigenvectors, we now turn our attention to plots of the modified relative sublattice displacement $\boldsymbol{u}$ and electrical field $\boldsymbol{E}$ as shown in Figs. 6–11. Since we are interested only in the envelope functions and relative magnitudes of the lateral and axial components of $\boldsymbol{u}$ and $\boldsymbol{E}$, in these figures we have used the simplified normalization conditions $\Lambda^{-1}\int \boldsymbol{u}^*\cdot\boldsymbol{u}dz=1$ and $\Lambda^{-1}\int \boldsymbol{E}^*\cdot\boldsymbol{E}dz=1$, in which the integral is over one period Λ.

First, let us focus on the displacement and electric field patterns for propagation in the lateral plane, i.e., $\theta=90°$. In this lateral propagation case, all the bulk phonon components shown in Eq. (3) are in phase. This means that their amplitudes $C^{L/T}_{\boldsymbol{q}}$ can all be set to be real which shall greatly facilitate our discussion and analysis. Also, according to Eq. (6) only those phonon modes whose wave vectors differ by an even number of superlattice wave vectors $\boldsymbol{q}_0$ will couple to each other. Therefore, the periodicity of the relative sublattice displacement $\boldsymbol{u}$ should be $\Lambda/2$ here.

The patterns for lateral propagation are shown in Figs. 6 and 7 for four different values of q, which are (A) $q\sim 0$ (long wave limit), (B) $q\sim 0.95q_0$ (just prior to the anticrossing), (C) $q\sim q_0$ (just after the anticrossing), and (D) $q\gg q_0$ (close to the BZ edge), respectively.

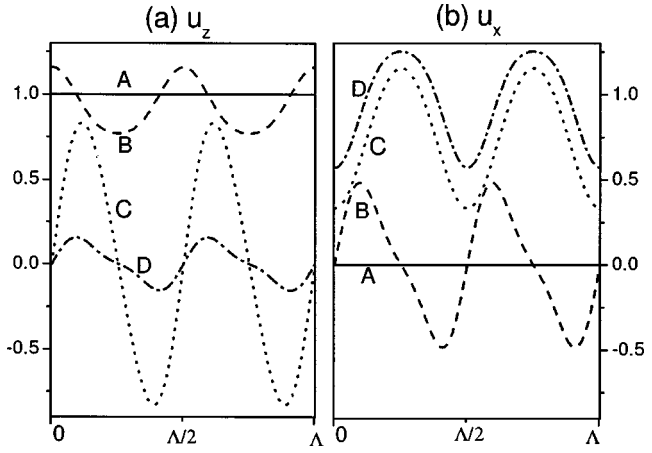

FIG. 6. Normalized sublattice displacement patterns over one period of PIPDS for $M=5$ and $\theta=90°$. (A) $q=0.0\times10^6$ cm^{-1}; (B) $q=20.0\times10^6$ cm^{-1}; (C) $q=22.2\times10^6$ cm^{-1}; (D) $q=110.5\times10^6$ cm^{-1}.

Now, let us start with the relative sublattice displacement patterns, shown in Fig. 6.

(A) In the very long wave limit $q\sim0$, as discussed in Sec. III, there exists only the axial component of the sublattices displacement, say $u_z=1$, while the lateral component $u_x=0$.

(B) Just prior to the anticrossing $q\sim0.95q_0$, according to Fig. 4(c) only the p-TO($\boldsymbol{q}$) and p-TO($\boldsymbol{q}\pm2\boldsymbol{q}_0$) modes are important. The p-TO($\boldsymbol{q}\pm2\boldsymbol{q}_0$) modes should have same weights (amplitude and phase) since they are symmetric to the p-TO($\boldsymbol{q}$) mode. If we label the weights of p-TO($\boldsymbol{q}$) and p-TO($\boldsymbol{q}\pm2\boldsymbol{q}_0$) modes as $C^T_{\boldsymbol{q}}$ and $C^T_{\boldsymbol{q}+2\boldsymbol{q}_0}$, respectively, then from Eq. (3) one can express the axial displacement as $u_z=C^T_{\boldsymbol{q}}+2C^T_{\boldsymbol{q}+2\boldsymbol{q}_0}\sin\theta_{\boldsymbol{q}+2\boldsymbol{q}_0,\boldsymbol{q}_0}\cos2q_0z$ and the lateral displacement as $\boldsymbol{u}_x=-i2C^T_{\boldsymbol{q}+2\boldsymbol{q}_0}\cos\theta_{\boldsymbol{q}+2\boldsymbol{q}_0,\boldsymbol{q}_0}\sin2q_0z$. One can see that $\boldsymbol{u}_z$ contains one constant term and one oscillating term, and, given that $\tan\theta_{\boldsymbol{q}+2\boldsymbol{q}_0,\boldsymbol{q}_0}\simeq0.5$, it is not difficult to see that the oscillating lateral term has twice the amplitude of the oscillating axial one.

(C) After the anticrossing $q\sim q_0$, the highest frequency mode becomes a combination of LO($\boldsymbol{q}$) and LO($\boldsymbol{q}\pm2\boldsymbol{q}_0$) modes. With similar considerations as in Case (B), the axial displacement becomes an odd function of z, $u_z=i2C^L_{\boldsymbol{q}+2\boldsymbol{q}_0}\cos\theta_{\boldsymbol{q}+2\boldsymbol{q}_0,\boldsymbol{q}_0}\sin2q_0z$ while the lateral displacement becomes an even function, $u_x=C^L_{\boldsymbol{q}}+2C^L_{\boldsymbol{q}+2\boldsymbol{q}_0}\sin\theta_{\boldsymbol{q}+2\boldsymbol{q}_0,\boldsymbol{q}_0}\cos2q_0z$. Using the fact that $\tan\theta_{\boldsymbol{q}+2\boldsymbol{q}_0,\boldsymbol{q}_0}\simeq0.5$, this time the amplitude of the u_z oscillating term is twice that of the lateral displacement u_x.

(D) As the wave vector increases towards the BZ bound-

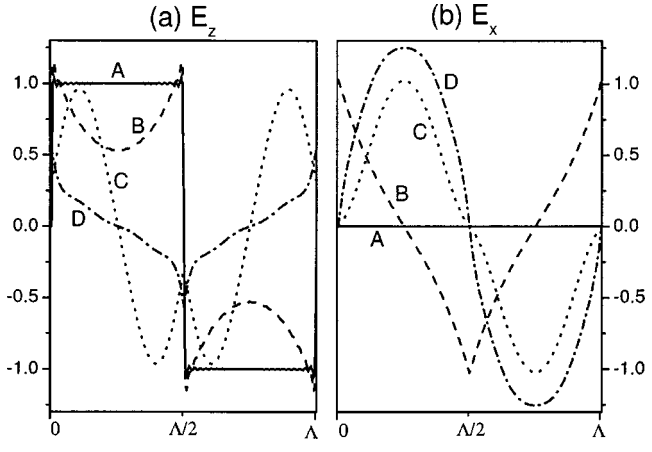

FIG. 7. Normalized electric field patterns over one period of PIPDS for $M=5$ and $\theta=90°$. (A) $q=0.0\times10^6$ cm^{-1}; (B) $q=20.0\times10^6$ cm^{-1}; (C) $q=22.2\times10^6$ cm^{-1}; (D) $q=110.5\times10^6$ cm^{-1}.

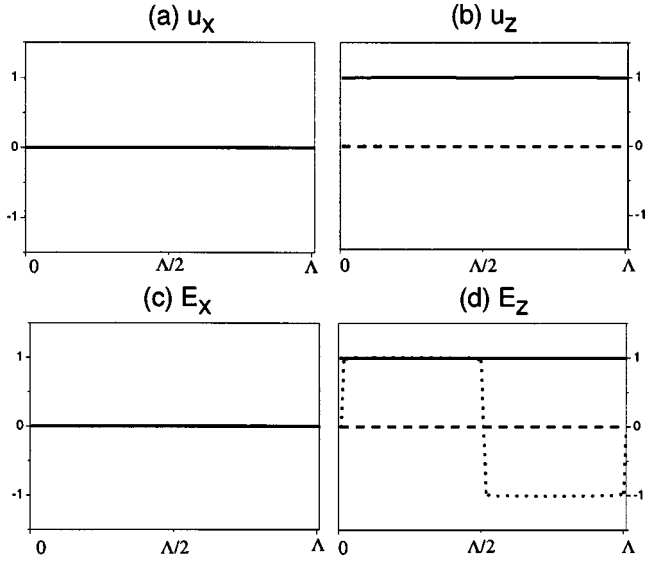

FIG. 8. Normalized sublattice displacement and electric field patterns in one period of PIPDS for $M=5$, $\theta=45°$, and $q=0.0\times10^6$ cm^{-1}. Imaginary, real parts, and absolute amplitude are drawn with dashed lines, dotted lines, and solid lines, respectively. The same rule will hold in Figs. 9–11.

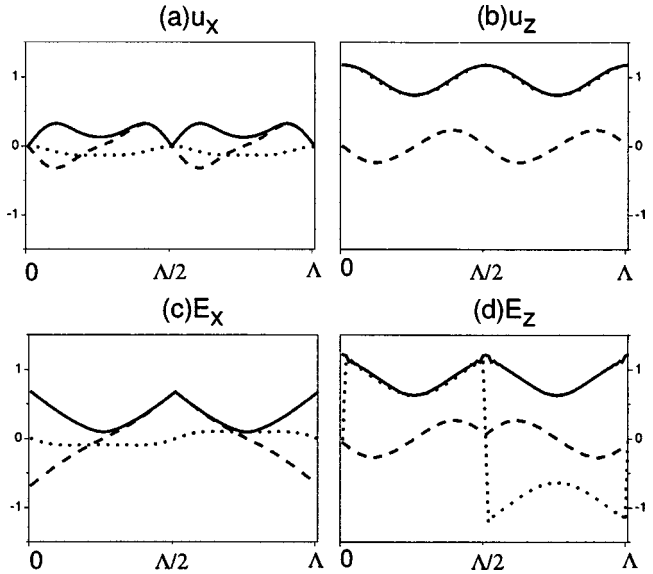

FIG. 9. Normalized sublattice displacement and electric field patterns in one period of PIPDS for $M=5$, $\theta=45°$, and $q=14.4\times10^6$ cm^{-1}.

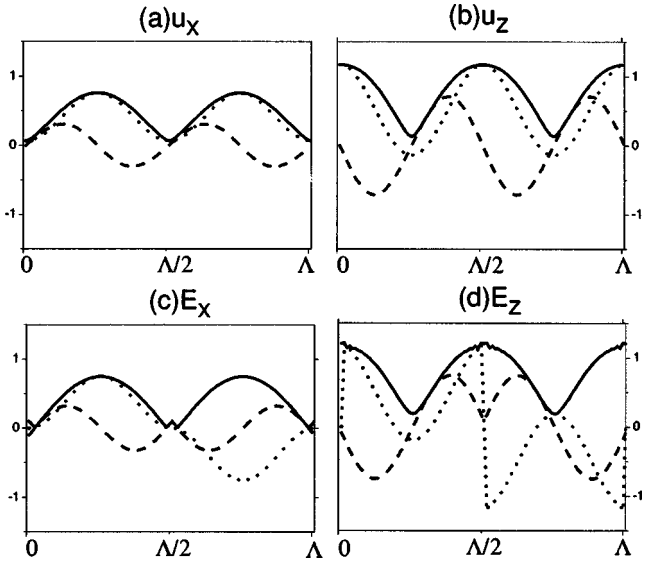

FIG. 10. Normalized sublattice displacement and electric field patterns in one period of PIPDS for $M=5$, $\theta=45°$, and $q=22.2\times10^6$ cm^{-1}.

ary, say $q \gg q_0$, the LO($\boldsymbol{q}$) becomes much more important, so that the axial displacement u_z and the oscillating amplitude of u_x all get smaller.

Next we turn our attention to the pattern of the electrical field $\boldsymbol{E}$ as shown in Fig. 7. From our former consideration and discussion, due to the periodical modulation function f, the periodicity of electric field $\boldsymbol{E}$ should be Λ and the symmetry of $\boldsymbol{E}$ should opposite to the symmetry of sublattice displacement $\boldsymbol{u}$, that is, if the displacement $\boldsymbol{u}$ is even, the electrical field should be odd, and vice versa. This is why the axial component of the electric field E_z can be discontinuous at the domain boundaries. This behavior is not in conflict with the electrical boundary conditions since only the normal component of the electric displacement D_z should be continuous at the interface. At the same time, the lateral component E_x is always continuous at the domain boundaries, as shown in Fig. 7(b). One should also note the small ripple seen in Fig. 7, which is an artifact of the finite number of terms used in the Fourier expansion in Eq. (5).

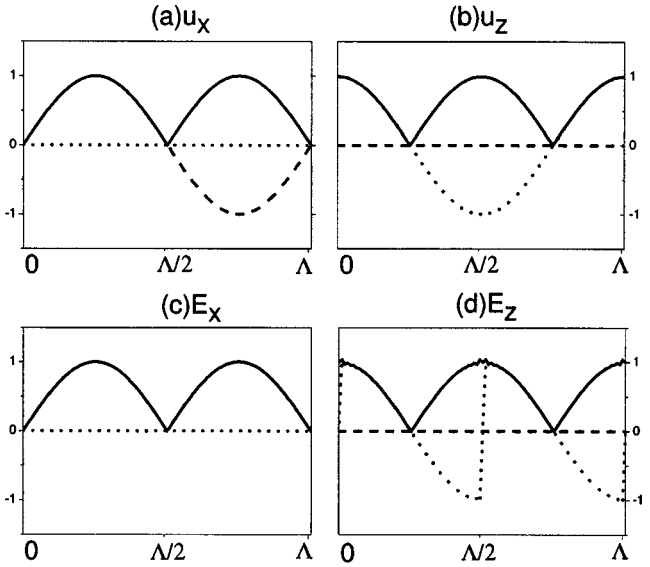

FIG. 11. Normalized sublattice displacement and electric field patterns in one period of PIPDS for $M=5$, $\theta=45°$, and $q=31.3\times10^6$ cm^{-1}.

The relative sublattice displacement and electrical field patterns are easy to visualize for the lateral propagation case since all the bulk phonon components are in phase with each other. With $\boldsymbol{q}$ along an arbitrary direction, the phase and amplitude relations become more complicated and both in-phase (real) and quadrature (imaginary) parts of each distribution pattern must be plotted. For $\boldsymbol{q}$ along the [101] direction ($\theta=45°$), the results are shown in Figs. 8–11. The imaginary, real parts, and absolute amplitude are drawn using dashed, dotted, and solid lines, respectively.

(A) In the long wave limit $q\sim0$ (Fig. 8), following the discussion in Sec. III, only the axial components of both sublattice displacement $\boldsymbol{u}$ and electric field $\boldsymbol{E}$ exist. The picture is identical to the long wave limit as shown in Figs. 6 and 7.

(B) As $\boldsymbol{q}$ increases towards the anticrossing (Fig. 9), the patterns change, and both in-phase and quadrature components of opposite symmetries arise. The periodicity of the sublattice displacement pattern remains $\Lambda/2$, while for the electrical field pattern it is still Λ.

(C) Past the anticrossing, the symmetries of the components change, but the periodicities remain, as shown in Fig. 10.

(D) The most interesting change of patterns occurs at the superlattice BZ edge, shown in Fig. 11. At this point, complete Bragg reflection takes place. Both axial and lateral displacements have the standing wave patterns. One can see indeed that u_x and u_z can be expressed as $u_x\sim\sin q_0 z$ and $u_z\sim\cos q_0 z$. As to the electrical field, the most striking characteristic is that the lateral electric field E_x does not average to zero here.

The main feature of all the patterns displayed in Figs. 6–11 is that the electric field patterns always have periodicity that is different from the relative sublattice displacement patterns. Since in polar materials, it is the electric field of optical phonon that is responsible for most of its interactions with electrons and photons, one should expect that these interactions undergo radical change in PIPDS. Of these interactions, the LO phonon scattering of hot electrons, the infrared absorption, and the Raman scattering of photons[9] are the ones that are of the most practical interest and they will be briefly considered in the next section.

V. INTERACTION WITH ELECTRONS AND PHOTONS

We have seen that periodic domain reversal can have a dramatic effect on the optical phonon spectrum of a zinc-blende semiconductor. Let us now turn our attention to the processes that lead to the creation and annihilation of these phonons and see how they are influenced by the domain reversal. In this brief description we shall concentrate on the selection rules rather than the magnitudes of the processes since the latter are not much different from those in bulk semiconductor.

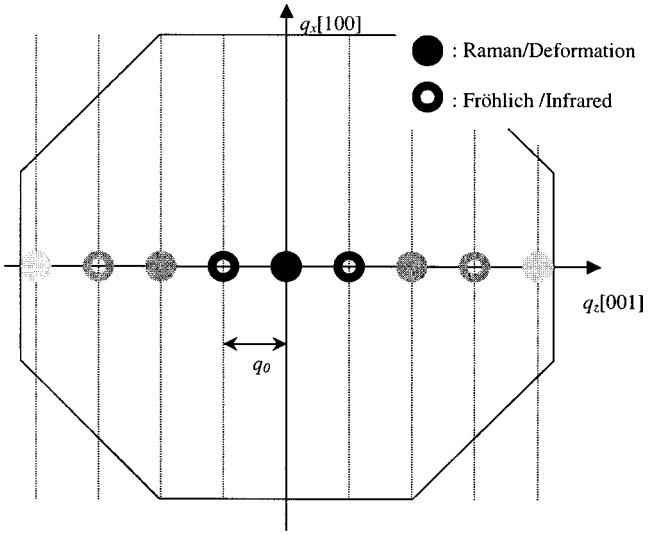

FIG. 12. Locations of scattered optical phonon through different processes. The importance of each position is labeled by the grayscale.

A. Fröhlich interaction

The scattering of hot carriers in polar semiconductors occurs mostly via the Fröhlich interaction, i.e., interaction between the electrons and electric field associated with LO phonons. The electric field in bulk semiconductors is

$$\boldsymbol{E} = -b_{21}\boldsymbol{u}/\varepsilon_0\varepsilon_\infty \sim \boldsymbol{E}_0 e^{i\boldsymbol{q}\cdot r - i\omega t}. \tag{14}$$

This electric field produces an electrostatic potential $\boldsymbol{\Phi}_{LO} \sim iq^{-1}\boldsymbol{E}_0 e^{i\boldsymbol{q}\cdot r - i\omega t}$. The interaction between the electrostatic potential $\boldsymbol{\Phi}_{LO}$ and the electron with initial wave vector $\boldsymbol{k}_i$ will scatter the electron into a new state $\boldsymbol{k}_f$ so that the energy and momentum are conserved, i.e., $\hbar^2(k_i^2-k_f^2)/2m_c = \pm\hbar\omega_{LO}(\boldsymbol{q})$ and $\boldsymbol{k}_i-\boldsymbol{k}_f=\pm\boldsymbol{q}$. Therefore, for the carriers near the BZ center, only the zone-center LO phonons can be generated, with the maximum LO wave vector being of the order of $q_{\max}\approx\sqrt{2m_c\omega_L/\hbar}\approx 2.4\times 10^6$ cm^{-1}.

The situation changes dramatically in PIPDS. The electric field now is $\boldsymbol{E}=-b_{21}f(z)\boldsymbol{u}/\varepsilon_0\varepsilon_\infty \sim \boldsymbol{E}_0\Sigma_{n=\pm1,\pm3\cdots} g_n e^{i(\boldsymbol{q}-n\boldsymbol{q}_0)\cdot\boldsymbol{r}-i\omega t}$, and it is not difficult to see that the momentum conservation condition for the Fröhlich scattering in PIPDS becomes $\boldsymbol{k}_i - \boldsymbol{k}_f=\pm[\boldsymbol{q}-n\boldsymbol{q}_0]$, where $n=\pm1,\pm3\ldots$. Thus Fröhlich scattering will generate optical phonons near the edge of the modified PIPDS BZ, with wave vectors $|\boldsymbol{q}-n\boldsymbol{q}_0|<q_{\max}$, i.e., inside a sphere of radius $q_{\max}$. These wave vectors are shown in Fig. 12 in an extended zone picture. The relative strengths of Fröhlich interaction, which are proportional to g_n^2, are shown by the darkness of the grayscale. Clearly, most of the scattering creates LO phonons with wave vectors near $\pm\boldsymbol{q}_0$.

It is instructive to estimate the average group velocity of the zone-edge optical phonons. Since according to the results of Sec. III B, the gap at the BZ edge along the z axis is very small and the LO phonons that are generated within a sphere of radius $q_{\max}$ will have a nonzero group velocity which can be estimated from

$$\langle v_{LO}^2\rangle \sim \frac{\int_{\boldsymbol{k}<\boldsymbol{q}_{\max}} |v(\boldsymbol{q}_0-\boldsymbol{k})|^2 d^3\boldsymbol{k}}{\int_{\boldsymbol{k}<\boldsymbol{q}_{\max}} d^3\boldsymbol{k}}. \tag{15}$$

A calculation for the highest energy branch shows that the average group velocity of the optical phonons for $M=5$ should be around 70 m/s in GaAs, while for $M=7$, it becomes 50 m/s. These values are much larger than the group velocities at the BZ center in bulk materials. With the lifetimes of LO phonons being the order of 10–100 ps,[14,15] one can see that the diffusion coefficient for the PIPDS zone-edge optical phonons is of the order of 10^{-3} cm^2 s^{-1} so that the diffusion length is of the order of a few nanometers. Therefore, one can possibly observe diffusion of the optical phonons in PIPDS. It is interesting to note that if we reduce M even further, the velocities of the optical phonons according to our model will increase to $\sim$300 m/s. However, this result must be taken with a grain of salt since PIPDS with such a very small period should be treated by more precise methods, such as microscopic models.

B. Deformation potential scattering

When it comes to scattering via the deformation potential scattering, the interaction Hamiltonian is proportional to the sublattice displacement $\boldsymbol{u}$ and is not modified by the periodic domain inversion. Therefore, optical phonons created via this process tend to be near the BZ center. Still, as shown in Secs. III and IV, the zone-center phonons in PIPDS are mixed (albeit weakly) with the phonons separated by an even number of superlattice wave vectors $\boldsymbol{q}_0$. The conservation of momentum for the deformation potential scattering thus becomes $\boldsymbol{k}_i-\boldsymbol{k}_f=\pm(\boldsymbol{q}-m\boldsymbol{q}_0)$, where $m=0,\pm2,\pm4\ldots$. The positions of the phonons created via the deformation potential scattering are also shown in Fig. 12.

C. Infrared absorption

As far as the optical properties, the main difference between PIPDS and a bulk zinc-blende lattice is the fact that the former does have a center of inversion located at the domain boundaries. Therefore, following the rule of mutual exclusion,[16] excitation that is active in the first-order infrared absorption spectrum is inactive in the first-order Raman spectrum. Indeed, let us consider the interaction between the infrared photon of frequency $\omega_p=\omega_{TO}$ and wave vector $\boldsymbol{k}_p$ and the phonon of wave vector $\boldsymbol{q}$. The interaction Hamiltonian is proportional to

$$\boldsymbol{E}_{\boldsymbol{k}_p}\cdot\boldsymbol{P}_{\boldsymbol{q}} \sim \boldsymbol{E}_{\boldsymbol{k}_p}\cdot b_{21}f(z)\boldsymbol{u}_{\boldsymbol{q}} \sim b_{21}\sum_{n=\pm1,\pm3,\ldots} g_n e^{in\boldsymbol{q}_0\cdot\boldsymbol{r}}\boldsymbol{E}_{\boldsymbol{k}_p}\cdot\boldsymbol{u}_{\boldsymbol{q}}, \tag{16}$$

where $\boldsymbol{P}_q$ is the ionic polarization associated with phonon. Therefore, momentum conservation for the infrared absorption becomes

$$\boldsymbol{q} - n\boldsymbol{q}_0 = \boldsymbol{k}_p \sim 0. \quad (17)$$

Thus infrared absorption generates only the TO phonons located near the modified PIPDS BZ edges, as shown in Fig. 12. It is these phonons that would also give rise to polaritons[9] in the PIPDS.

D. Raman scattering

As we have already mentioned, from a symmetry point of view, the BZ edge phonons active in the infrared should be inactive in Raman spectra, and only the BZ-center LO and TO phonons should contribute to Raman spectra, just as in the bulk material. Of course, for the case when the Raman scattering is caused by the deformation potential, this observation is obvious since the domain inversion hardly causes any change in the mechanical properties. For the case when Raman scattering is caused by the electric field of LO phonons, this result can also be understood rather easily from the following simple considerations. The electric field of the long wavelength LO phonon $\boldsymbol{E} = -b_{21} f(z)\boldsymbol{u}/\varepsilon_0\varepsilon_\infty$ reverses its sign at the domain boundary. So does the linear electro-optic coefficient $\partial\chi/\partial\boldsymbol{E} \sim f(z) r_{14,bulk}$. Therefore, the phonon-induced variation of the optical susceptibility, $(\partial\chi/\partial\boldsymbol{u})_0\boldsymbol{u} \sim -b_{21} r_{14,bulk}\boldsymbol{u}/\varepsilon_0\varepsilon_\infty$, does not change its sign at the boundary. The PIPDS thus behaves almost entirely like the bulk materials with a small exception — the BZ center optical phonons are weakly mixed with the optical phonons separated by even number of superlattice wave vector $\boldsymbol{q}_0$. Therefore, the selection rule for the Raman scattering is $\boldsymbol{k}_{p,i} - \boldsymbol{k}_{p,s} = \pm(\boldsymbol{q} - m\boldsymbol{q}_0)$, with m being the even integers, and is also as shown in Fig. 12.

Figure 12 shows the locations of optical phonons generated by all possible electronic and optical interactions. As can be seen, due to the inversion symmetry of PIPDS, the locations are complimentary—all the phonons generated by deformation potential or Raman scattering are located in the vicinity of the BZ centers while all the phonons generated by Fröhlich scattering and infrared absorption are located near BZ edges.

VI. CONCLUSIONS

In this work we have considered the properties of optical phonons in a periodically inverted polar domain structure — the small-scale equivalent of the quasi-phase-matched periodically poled domain structures in nonlinear optics. We have calculated the dispersion of optical phonons and described their main features. These include zone folding and the mixing of LO/TO modes separated by even number of superlattice wave vector $\boldsymbol{q}_0$. We have also obtained the patterns of sublattice displacement and electric field associated with the phonons and shown that in the wave-vector space the electric field $\boldsymbol{E}$ is always shifted relative to the sublattice displacement $\boldsymbol{u}$ by an odd number of superlattice wave vectors $\boldsymbol{q}_0$. We have also briefly considered the interactions of PIPDS phonons with electrons and photons and obtained modified selection rules for various processes.

As far as the potential application of PIPDS, the first one that comes to mind is to use them in order to excite the optical phonons away from the BZ center. Furthermore, in short-period PIPDS, optical phonons interacting with electrons will have higher diffusion coefficients and thus be able to quickly diffuse away to provide effective cooling channels for high-speed semiconductor devices. However, to analyze such structures one needs to use methods more precise than what we have developed here, which will be the emphasis of our future work.

ACKNOWLEDGMENT

This work is supported by the AFOSR under Contract No. F49620-00-1-0328 through the MURI program.

[1] J. Y. Tsao, *Materials Fundamentals of Molecular Beam Epitaxy* (Academic, Boston, 1993).
[2] B. R. Nag, *Physics of Quantum Well Devices* (Kluwer, Boston, 2000); V. V. Mitin, V. A. Kochelap, and M. A. Stroscio, *Quantum Heterostructures: Microelectronics & Optoelectronics* (Cambridge, New York, 1999).
[3] W. Potz and P. Kocevar, in *Hot Carriers in Semiconductor Nanostructures: Physics and Application*, edited by J. Shah (Academic, Boston, 1992).
[4] B. K. Ridley, *Electrons and Phonons in Semiconductor Multilayers* (Cambridge, New York, 1997).
[5] M. A. Stroscio and M. Dutta, *Phonons in Nanostructures* (Cambridge, New York, 2001).
[6] C. Trallero-Giner, R. Pérez-Alvarez, and F. García-Moliner, *Long Wave Polar Modes in Semiconductor Heterostructures* (Pergamon/Elsevier Science, London, 1998).
[7] M. M. Fejer, Phys. Today **47** (5), 25 (1994).
[8] L. A. Eyres, P. J. Tourreau, T. J. Pinguet, C. B. Ebert, J. S. Harris, M. M. Fejer, L. Becouarn, B. Gerard, and E. Lallier, Appl. Phys. Lett. **79**, 904 (2001).
[9] P. Y. Yu and M. Cardona, *Fundamentals of Semiconductors: Physics and Materials Properties* (Springer, Berlin, 1996).
[10] M. Krejci, A. N. Tiwari, H. Zogg, P. Schwander, H. Heinrich, and G. Kostorz, J. Appl. Phys. **81**, 6100 (1997).
[11] D. R. Rasmussen, S. McKernan, and C. B. Carter, Phys. Rev. Lett. **66**, 2629 (1991).
[12] J. C. Philips, *Bonds and Bands in Semiconductors* (Academic, New York, 1973).
[13] M. Born and K. Huang, *Dynamical Theory of Crystal Lattices* (Oxford, New York, 1988), p. 82.
[14] F. Vallee, Phys. Rev. B **49**, 2460 (1994).
[15] A. Debernardi, Phys. Rev. B **57**, 12 847 (1998).
[16] M. Balkanski, *Optical Properties of Semiconductors* (Elsevier, New York, 1994).
[17] F. de Leon-Pérez and R. Pérez-Alvarez, Phys. Rev. B **62**, 9915 (2000); O. Madelung, *Semiconductors—Basic Data*, 2nd ed. (Springer, New York, 1996), p. 108. LST is assumed to be satisfied.